RSC Advances

ROYAL SOCIETY OF CHEMISTRY

PAPER

View Article Online
View Journal | View Issue



Cite this: *RSC Adv.*, 2025, **15**, 32995

# Exploring the antibacterial properties of ZnO nanorods–CuO nanoflowers: a mode of action approach

Vijay S. Ghodake,[ab] Pramod A. Koyale,[c] Satyajeet S. Patil,[d] Pramod S. Patil[de] and Sagar D. Delekar*[a]

This study presents an innovative approach to enhancing the antibacterial performance of zinc oxide nanorods (ZnO NRs) by functionalizing them with copper oxide nanoflowers (CuO NFs). Initially, ZnO NRs were synthesized using a straightforward sol–gel wet chemical method, followed by the controlled integration of CuO NFs to form the desired ZnO–CuO nanocomposites (ZC NCs). Detailed physicochemical characterization tools were employed to interpret the associated structural, functional, optical, and morphological properties of the synthesized samples. X-ray diffraction (XRD) analysis was further quantitatively supported by Rietveld refinement, providing a brief account of the structural parameters and other aspects. Herein, the augmented antibacterial performance can be understood by observing the improved surface area determined by Brunauer–Emmett–Teller (BET) analysis, which shows a higher surface area of 187.622 $m^2$ $g^{-1}$ compared to bare ZnO NRs, exhibiting a high surface area-to-volume ratio that facilitates extensive contact with microbes. Notably, ZC NCs (50 wt% of CuO NFs with ZnO NRs) demonstrated significant antimicrobial activity against *S. aureus*, *B. cereus*, *E. coli*, *P. aeruginosa*, and *C. albicans*. Additionally, the mode of action study revealed that the antimicrobial performance is primarily attributed to the generation of reactive oxygen species (ROS) and the disruption of the microbial cell membrane. These dual-functional ZC NCs demonstrate significant potential in healthcare applications, providing a cost-effective and scalable solution for developing advanced antibacterial and antifungal agents.

Received 10th June 2025
Accepted 11th August 2025

DOI: 10.1039/d5ra04095g

rsc.li/rsc-advances



## Introduction

The global mortality rate is rising due to the rapid expansion of bacterial and fungal infections and the widespread presence of resistant microbes. By 2050, it is predicted that up to 10 million people will die annually from these infections, with treatment costs approaching USD 100 trillion. In 2014, the World Health Organization (WHO) identified the growth of antimicrobial-resistant microbes as a serious threat to global health. Factors such as the misuse and overuse of antimicrobial agents, agricultural antibiotic use, and increased global travel contribute significantly to the spread of antimicrobial resistance.[1,2]

Addressing this pressing healthcare challenge requires the development of new strategies and approaches. Antimicrobial agents are broadly categorized into organic and inorganic types. Organic antimicrobial agents have several drawbacks. They are less stable, degrading more quickly when exposed to light or heat, and generally have lower potency. Their effectiveness can significantly depend on environmental conditions, and their production costs are often high.[3,4] Additionally, they can cause allergic reactions in some individuals. Conversely, inorganic antimicrobial agents are generally more stable and durable than their organic counterparts. They are effective against a wide range of microorganisms, including bacteria, fungi, and viruses. When used appropriately, many inorganic agents are non-toxic to humans and environmentally safe.[5]

Modern advances in nanotechnology have provided new approaches to constructing inorganic antimicrobial agents with higher efficacies. Numerous studies have shown that multi-drug resistant bacteria, both Gram-positive and Gram-negative, cannot grow as quickly when exposed to inorganic antimicrobial agents such as zinc oxide nanorods (ZnO NRs), copper oxide nanoflowers (CuO NFs),[6,7] silver metal (Ag),[6,8] nickel oxide (NiO),[9,10] titania nanoparticles ($TiO_2$ NPs),[11,12] $TiO_2$-based nanocomposites (NCs),[13,14] ZnO-based NCs,[15–18] *etc.* In this

[a]*Department of Chemistry, Shivaji University, Kolhapur 416 004, Maharashtra, India. E-mail: sdd_chem@unishivaji.ac.in*
[b]*Department of Chemistry, Yashwantrao Chavan Mahavidyalaya, Halkarni, Kolhapur, 416 552, Maharashtra, India*
[c]*School of Nanoscience and Biotechnology, Shivaji University, Kolhapur 416 004, Maharashtra, India*
[d]*Thin Film Materials Laboratory, Department of Physics, Shivaji University, Kolhapur 416 004, Maharashtra, India*
[e]*National Dong Hwa University, Hualien, 974 301, Taiwan*

context, ZnO NRs have emerged as promising candidates due to their unique physicochemical properties and potent antimicrobial activity.[19] ZnO NR is a wide-bandgap (3.14 eV) semiconductor material known for its high stability, biocompatibility, and effectiveness against a wide range of microbes.[20] At proper concentrations, it is safe for people to use and produces reactive oxygen species (ROS) under various conditions, which increases its antibacterial effectiveness. It works by breaking down microbial cell walls, producing ROS, and releasing $Zn^{2+}$ ions, all of which lead to the death of bacterium cells.[21,22]

Several studies have highlighted the potent antibacterial activity of highly crystalline and monodispersed ZnO NRs. For instance, Babayevska Nataliya *et al.* reported that ZnO NRs exhibit significantly stronger antibacterial effects against *E. coli* and *S. aureus* compared to ZnO microparticles, largely due to their high specific surface area. Additionally, research by N. Babayevska *et al.* demonstrated that 70% of cells showed damage to the cytoplasmic membrane after just 15 min of exposure to ZnO NRs, with this antimicrobial activity evaluated using the resazurin microtiter assay (REMA).[21] Furthermore, E. Takele *et al.* found that crystalline ZnO NRs are particularly effective against *B. subtilis* (a Gram-positive bacterium) compared to *E. coli* and *Pseudomonas* bacteria (both Gram-negative).[23] Despite their promising antimicrobial properties, ZnO NRs have certain limitations and challenges, such as photostability and limited targeting specificity. Typically, they exhibit non-specific antimicrobial activity, affecting both harmful pathogens and beneficial microbes, which can potentially disrupt natural microbial ecosystems.[24,25]

To address these limitations, this study investigates the competent antibacterial synergy achieved by functionalizing ZnO NRs with CuO NFs. When combined in NCs, these materials often exhibit synergistic antibacterial properties.[26,27] CuO NFs offer several advantages over ZnO NRs alone, including their unique flower-like structure, which provides a high surface area for enhanced reactivity. This structure facilitates efficient ROS generation, which can damage critical bacterial cell components such as proteins, lipids, and DNA. Additionally, CuO NFs release copper ions ($Cu^{2+}$) with strong antimicrobial activity. The synthesis of these composites is relatively simple and cost-effective, and they display good stability and durability under various environmental conditions.[28] CuO NFs contribute bactericidal properties that improve the overall efficacy of the NCs against a broader range of pathogens. ZnO–CuO (ZC) NCs also exhibit lower cytotoxicity compared to bare ZnO NRs at equivalent concentrations.[29] The dual functionality of ZC NCs enables targeted antimicrobial action, while their enhanced stability and controlled release properties may result in prolonged antimicrobial effectiveness.[30,31]

Several studies support these findings. Derazkola Sobhan Mortazavi *et al.* reported that ZC NCs exhibit a spherical morphology and demonstrate excellent antifungal and antibacterial activity.[32] R. Azouani *et al.* tested the antibacterial effect of ZC NCs coated on shoe insoles against *S. aureus*, finding that insoles coated with 0.35 wt% ZC NCs exhibited significant antibacterial activity.[1] Similarly, M. N. Mydin *et al.* explored the antimicrobial properties of ZC NCs against *S. aureus*, *E. coli*, *K. pneumoniae*, and *P. aeruginosa*, highlighting their broad-spectrum efficacy.[29] G. Nagaraju *et al.* conducted antibacterial studies against *E. coli* and *S. aureus*, demonstrating substantial zones of inhibition, with efficacy comparable to the standard antibiotic ciprofloxacin.[33] Additionally, B. Abebe *et al.* successfully synthesized ZC NCs, supporting that incorporating ZnO with CuO enhances crystallinity, increases ROS generation, and ultimately improves antibacterial activity.[34] While the antibacterial efficacy of ZC NCs has been extensively studied, several challenges remain, including limited comparisons with standard antibiotics, variations in morphology and size, stability issues, interactions with biological systems, and an unclear mechanism of ROS generation.

So, the present work aims to address these limitations by investigating the synthesis, characterization, and antibacterial properties of ZC NCs in greater detail. The antibacterial efficacy of ZC NCs was evaluated against clinically relevant bacterial strains, including *S. aureus*, *B. cereus*, *E. coli*, and *P. aeruginosa*, as well as the fungal strain *C. albicans*. Additionally, the study explored the mechanisms underlying microbial inhibition, such as bacterial cell wall disruption, as evidenced by microscopic images. Cytotoxicity assessments and morphological studies further confirmed the potential of ZC NCs for biomedical and environmental applications. Overall, the enhanced antibacterial properties of ZC NCs make them promising candidates for various applications, including coatings for medical devices and implants, wound dressings, and surface coatings.

## Results and discussion

### X-ray diffraction (XRD) pattern analysis

The structural properties of all samples were investigated by using XRD patterns as depicted in Fig. S1 in the SI. The XRD pattern of ZnO NRs was matched with the JCPDS card number 89-1397.[35] ZnO NRs exhibit the characteristic peaks at $2\theta$ = 31.79°, 34.44°, 36.20°, 47.47°, 56.62°, 62.79°, and 69.13° that are attributed to the (100), (002), (101), (102), (110), (113), and (112) crystalline planes, respectively.[35] In addition, the representative peaks at $2\theta$ = 5.56°, 38.70°, and 66.26° within XRD patterns of ZC 50 NCs signify CuO NFs (*) with ZnO lattice.

However, the weak intensity of CuO NFs in XRD patterns may be attributed to several factors. Primarily, the surface-deposited CuO NFs likely possess lower crystallinity or smaller crystallite size, leading to broader and less intense diffraction peaks relative to the well-crystallized ZnO NRs. Furthermore, since CuO exists predominantly as a surface layer rather than as a bulk phase, its contribution to the overall diffraction signal is inherently limited. These aspects were supported through Rietveld refinement, providing more correlated insights for the actual metal oxide composition within the nanocomposite. Rietveld refinement is performed using Fullprof software for bare ZnO NRs (Fig. 1a), CuO NFs (Fig. 2a), and all ZC NCs [Fig. 3a–d]. The 1011258 (ZnO NRs) and 9016326 (CuO NFs) CIF files from the COD website are used. For Rietveld analysis, the

 

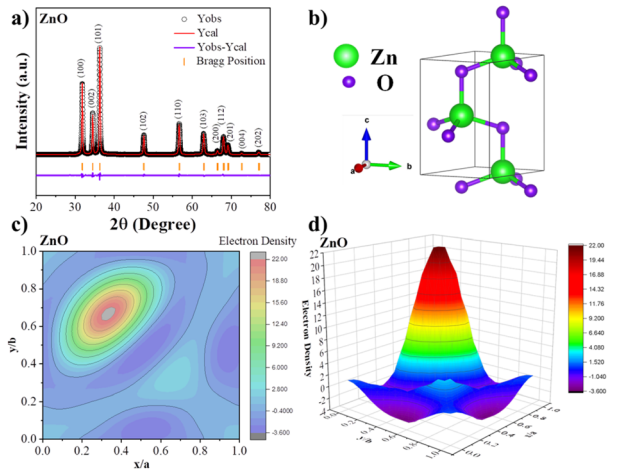


Fig. 1 (a) Rietveld refined XRD pattern, (b) unit cell crystal structure, and (c and d) 2D and 3D electron density map of a unit cell of ZnO NRs.

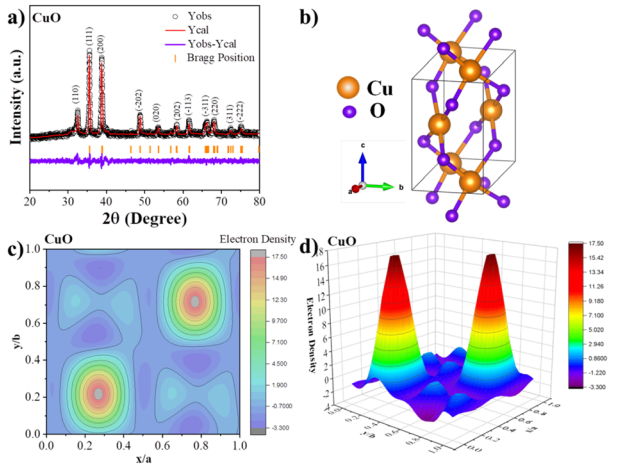


Fig. 2 (a) Rietveld refined XRD pattern, (b) unit cell crystal structure, and (c and d) 2D and 3D electron density map of a unit cell of CuO NFs.

pseudo-Voigt peak profile is employed. Chi-square ($\chi^2$) values and quality of fit are calculated as follows.[36]

$$\chi^2 = \left(\frac{R_{wp}}{R_{exp}}\right)^2$$

$$S = \left(\frac{R_{wp}}{R_{exp}}\right)$$

Tables 1 and S2, SI reveal various structural and refinement parameters obtained after the Rietveld analysis. All the refined parameters are within an acceptable range. The crystal structure of ZnO NRs, CuO NFs, and ZC 50 NCs was generated using VESTA software, presented in Fig. 1b, 2b, and 3e, respectively. Furthermore, 2D and 3D electron density plots for bare ZnO NRs [Fig. 1c and d] and CuO NFs [Fig. 2c and d] were plotted using the Fourier transform to understand the electron density distribution inside a unit cell.

The XRD analysis provides critical insights into the crystalline structure and phase composition of the NCs, which significantly influence their antibacterial activity. The presence of sharp and well-defined diffraction peaks indicates high crystallinity, a key factor in facilitating the generation of ROS upon interaction with microbial cells a primary mechanism of

Table 1 Various Rietveld refinement parameters of all the ZC samples

| Sample code | $\chi^2$ | $S$ | $R_{wp}$ | $R_{exp}$ | $R_p$ | $R_B$ (%) | $R_F$ (%) |
|---|---|---|---|---|---|---|---|
| ZnO | 1.59 | 1.26 | 6.54 | 5.18 | 6.11 | 3.58 | 4.70 |
| ZC 10 | 2 | 1.41 | 17.6 | 12.42 | 16.8 | 9.62 | 12.4 |
| ZC 20 | 1.95 | 1.39 | 21.1 | 15.10 | 23.6 | 8.96 | 11.6 |
| ZC 30 | 2.08 | 1.44 | 19.00 | 13.19 | 20.20 | 8.82 | 11.4 |
| ZC 50 | 2.17 | 1.47 | 21.1 | 14.30 | 22.9 | 8.37 | 11.00 |
| CuO | 1.54 | 1.24 | 31.40 | 25.32 | 51.70 | 6.04 | 7.77 |

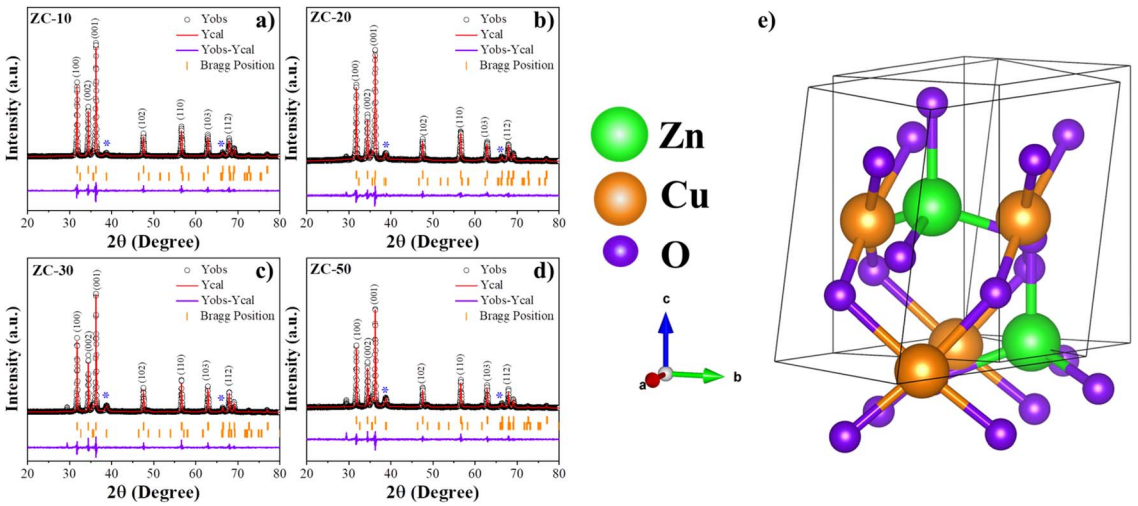


Fig. 3 Rietveld refined XRD patterns of (a) ZC 10 NCs, (b) ZC 20 NCs, (c) ZC 30 NCs, and (d) ZC 50 NCs. (e) Unit cell crystal structure of ZC NCs.

bacterial inactivation. Additionally, the calculated crystallite size suggests nanoscale dimensions that contribute to an increased specific surface area, enhancing the contact between nanomaterials and bacterial membranes. Smaller crystallites are often associated with a higher density of surface defects, which aid in effective electron–hole pair separation, thereby intensifying oxidative stress on microbial cells and leading to improved antibacterial performance.[37,38]

### Fourier transform infrared (FT-IR) analysis

Fig. 4a presents the FT-IR spectra of all samples, measured in the 4000–400 $cm^{-1}$ range at room temperature. For the bare ZnO NRs, broad absorption bands between 433 and 600 $cm^{-1}$ are observed, which are attributed to the Zn–O and Zn–O–Zn bonding vibrations.[39] A similar pattern is seen for the bare CuO NFs, where the bands in this range correspond to Cu–O bonds.[40] In the case of ZC 50 NCs, an additional characteristic peak appears at 1106 $cm^{-1}$, which can be attributed to the presence of CuO NFs and is associated with the M–OH bond. Upon incorporating CuO NFs into the ZnO lattice, a decrease in the intensity of the M–OH peak is observed, while the intensity of the broad absorption band between 3000 and 3500 $cm^{-1}$ increases, likely corresponding to O–H stretching vibrations. This shift suggests an interaction between ZnO and CuO, highlighting the structural and functional connectivity within the ZC 50 NCs, which aligns well with the properties of the bare ZnO NRs.[32] In addition, FT-IR spectra of optimized ZC 10, ZC 20, and ZC 30 NCs are given in Fig. S2, SI.

### UV-visible diffuse reflectance spectroscopy (UV-visible DRS) analysis

Fig. 4b and c displays the UV-visible DRS and Tauc plot of bare ZnO NRs, CuO NFs, and ZC 50 NCs. The spectra reveal the absorption edge for ZnO NRs limited to the UV region, CuO, which was further enhanced upon the incorporation with CuO NFs, suggesting an improvement in the material's optical properties. This enhancement is reflected in the reduced band gap of 2.37 eV for ZC 50 NCs, compared to 3.12 eV for bare ZnO NRs, as determined from the Tauc plot. The UV-visible DRS spectra for other samples and their associated band gap values with band edges are shown in Fig. S3, SI, and mentioned in Table S3, SI. So, such a combination of ZnO NRs with CuO NFs significantly strengthens the material's absorption in the visible region, which in turn supports the generation of ROS under visible light irradiation, ultimately contributing to enhanced antibacterial activity.[41]

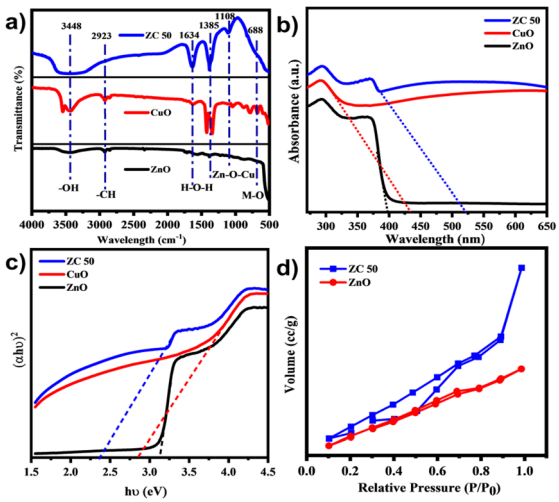


Fig. 4 (a) FT-IR spectra, (b) UV-visible DRS, (c) Tauc plots for bare ZnO NRs, CuO NFs, and ZC 50 NCs. (d) $N_2$ adsorption–desorption isotherms of bare ZnO NRs, and ZC 50 NCs.

### Brunauer–Emmett–Teller (BET) analysis

Fig. 4d and S4, SI depict the $N_2$ adsorption–desorption isotherms and Barrett–Joyner–Halenda (BJH) pore size distribution analyses for ZnO NRs and ZC 50 NCs, respectively. These results indicate that ZC 50 NCs possess a significantly higher surface area (187.622 $m^2\ g^{-1}$) and larger pore size distribution (ranging from 1.813 to 2.317 nm) compared to bare ZnO, suggesting both microporous and mesoporous characteristics.[42] Table 2 summarizes these parameters. The increased surface area and pore size of ZC 50 NCs likely facilitate enhanced microbial anchoring and improved interaction with microbial cells, contributing to its superior antimicrobial efficacy.[3] The enhanced surface area observed in the ZC NCs results from the combined contributions of the ZnO NRs and the surface-deposited CuO NFs. While, this comparison does not deconvolute the individual contributions of ZnO NRs and CuO NFs, intending to reflect the cumulative enhancement and its relevance to the observed improvement in antibacterial performance. This enhancement is noteworthy when compared to other reported antimicrobial ZnO-based NCs such as Zn–CuO (168.00 $m^2\ g^{-1}$),[43] ZnO/Ag (18.20 $m^2\ g^{-1}$),[44] CuO/ZnO (23.20 $m^2\ g^{-1}$)[45] and CuO/Ag (18.00 $m^2\ g^{-1}$),[44] *etc.* supporting our claim of achieving an optimal specific surface area. The high defect density and numerous active sites further suggest that these NCs are promising for applications requiring robust antimicrobial and antioxidant properties.[41]

### Morphology and elemental composition analyses

Fig. 5a–c presents field emission scanning electron microscopy (FESEM) images depicting the structural morphologies of ZnO and ZC 50 NCs.

In Fig. 5a, ZnO holds hexagonal, rod-like nanostructures, characterized by a high surface area-to-volume ratio, revealing the morphology of NRs. The associated histogram for ZnO NRs is shown in Fig. S5, SI. Fig. 5b illustrates NFs associated with the

Table 2 The observed value of specific surface area, pore size, and pore volume of the bare ZnO NRs and ZC 50 NCs

| Sample | Specific surface area ($m^2\ g^{-1}$) | Pore size (nm) | Pore volume ($cm^3\ g^{-1}$) |
|---|---|---|---|
| ZnO NRs | 68.547 | 1.813 | 0.441 |
| ZC 50 NCs | 187.622 | 2.317 | 0.680 |

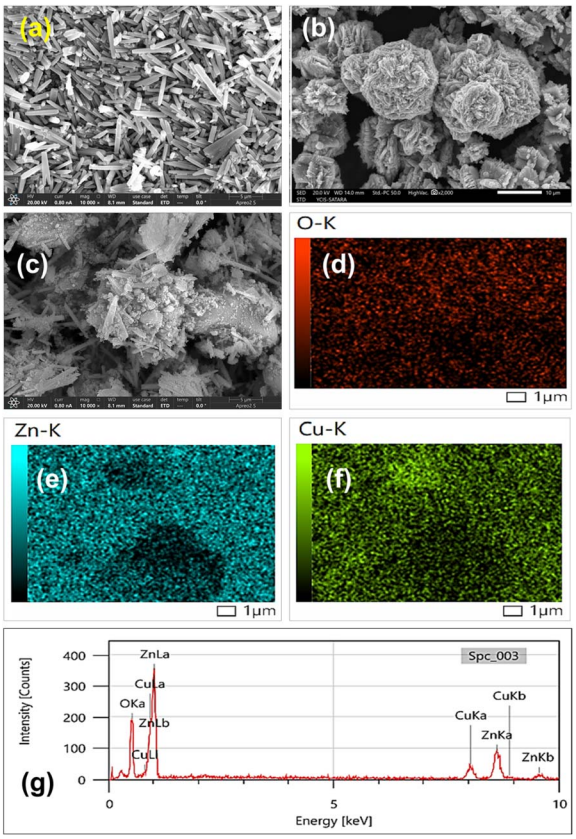


Fig. 5 FESEM images of (a) bare ZnO NRs, (b) CuO NFs, and (c) ZC 50 NCs. (d–f) Elemental mapping images for O, Zn, and Cu elements. (g) EDS of ZC 50 NCs.

CuO sample. Thereafter, Fig. 5c shows the composed structure of ZnO NRs and CuO NFs, having heterogeneous morphology with widely distributed particle sizes, which makes it difficult to definitively resolve individual features. This heterogeneity arises due to the surface decoration of CuO NFs over ZnO NRs, which leads to irregular agglomeration and a complex surface texture in the final NCs. These structural features promote extensive contact with microbes, enhancing antimicrobial activity by facilitating mechanical disruption of microbial cell membranes.[46] Afterward, Fig. 5d–f shows elemental mapping images for elemental O, Zn, and Cu. The high surface area and sharp edges of the ZnO NRs within the ZC 50 NCs significantly enhance antimicrobial efficacy by increasing microbial inhibition.[21] Hence, the FESEM images visually emphasize the unique nanostructures and morphologies crucial to the ZC 50 NCs' antimicrobial performance.

In addition, the elemental composition analysis of the ZC 50 NCs was performed *via* energy-dispersive X-ray spectroscopy (EDS), as shown in Fig. 5g. Elemental analysis confirms the presence of Zn, Cu, and O in the ZC 50 NCs, with no extraneous peaks detected, affirming the purity of the synthesized materials as well as showing that these Zn, Cu, and O species are homogeneously distributed throughout the entire selected area of ZC 50 NCs, as already supported by elemental mapping images. Comparing the EDS analysis of ZC 50 NCs to that of reported EDS for bare ZnO NRs validates the targeted elemental composition,[47] underscoring the potential of ZC 50 NCs in antimicrobial applications.

## Biocompatibility study

**Cytotoxicity study.** Fig. 6 illustrates the cytotoxic effects on fibroblast cells (L929) following exposure to ZC 50 NCs. human fibroblast cells lines (L929) procured from the National Centre for Cell Science (NCCS), Pune, India. L929 fibroblast cells were cultured at a density of $1 \times 10^4$ cells per mL in complete growth medium and incubated for 24 h at 37 °C in a humidified atmosphere containing 5% $CO_2$. Following this initial incubation, 100 μL of the cell suspension (equivalent to $1 \times 10^4$ cells per well) was seeded into 96 well tissue culture-grade microplates. After allowing sufficient time for cell attachment, various concentrations of the test samples (2, 4, 6, 8, and 10 μg $mL^{-1}$) were added to the wells in 100 μL of fresh medium. Control wells were treated with 0.2% DMSO [dimethyl sulfoxide] in PBS [phosphate-buffered saline] and served as solvent controls. All experimental groups, including controls, were prepared in triplicate to ensure reproducibility and statistical reliability. The plates were then incubated for an additional 24 h under standard culture conditions (37 °C, 5% $CO_2$). After incubation, the culture medium was carefully removed, and 20 μL of MTT reagent (5 mg $mL^{-1}$ in PBS) was added to each well. The plates were incubated for a further 4 h at 37 °C to allow viable cells to reduce the yellow MTT to insoluble dark purple formazan crystals, which were confirmed microscopically. Following crystal formation, the MTT-containing medium was removed, and 200 μL of DMSO was added to each well to solubilize the formazan. The plates were incubated for 10 min at 37 °C, protected from light using aluminium foil. Finally, absorbance was measured at 550 nm using a microplate reader, and the data

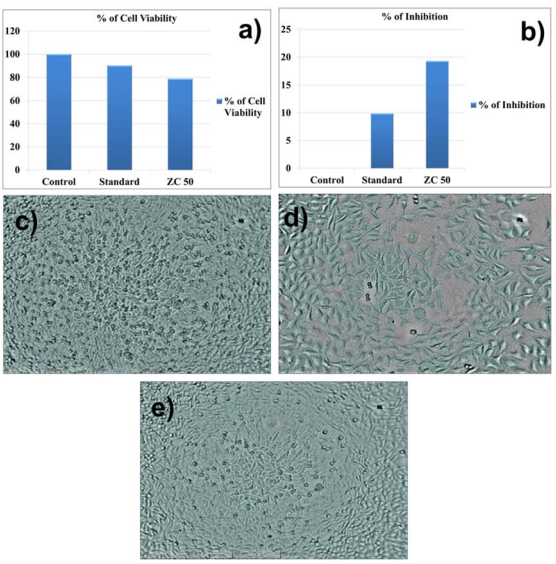


Fig. 6 Cytotoxicity of fibroblast cell line following exposure to the ZC 50 NCs (a) % of cell viability, (b) % of inhibition, and cellular morphology: (c) control (d) standard, and (e) ZC 50 NCs.

Table 3 Effects of compound against L929 fibroblast cell line by MTT assay

| Sr. no. | Sample code | Concentration (μg mL$^{-1}$) | OD | % of viability (%) | % of inhibition (%) | IC50 (μg mL$^{-1}$) |
|---|---|---|---|---|---|---|
| 1 | Control (lactic acid) | — | 1.114 | — | — | — |
| 2 | Standard | 2 | 1.004 | 90.12% | 9.87% | NE |
| | | 4 | 0.997 | 89.49% | 10.50% | |
| | | 6 | 0.970 | 87.07% | 12.92% | |
| | | 8 | 0.954 | 85.63% | 14.36% | |
| | | 10 | 0.933 | 83.75% | 16.24% | |
| 3 | ZC 50 | 2 | 0.990 | 88.86% | 11.13% | NE |
| | | 4 | 0.983 | 86.22% | 11.75% | |
| | | 6 | 0.971 | 87.16% | 12.83% | |
| | | 8 | 0.962 | 86.35% | 13.64% | |
| | | 10 | 0.945 | 84.82% | 15.17% | |

obtained from triplicate samples were analyzed to determine cell viability relative to the control.

Based on the results of the cytotoxicity study, it can be concluded that the synthesized ZC 50 NCs exhibit minimal toxicity toward human fibroblast cells (L929). This indicates a favourable biocompatibility profile, suggesting that ZC 50 NCs is safe for potential use in biomedical applications. The low cytotoxicity makes these NCs promising candidates for incorporation into medical devices, drug delivery systems, wound healing materials, and other healthcare-related technologies. Their compatibility with human cells supports their potential to enhance therapeutic efficacy while reducing the risk of adverse effects, thereby contributing to safer and more effective biomedical solutions. Table 3 presents the cytotoxic effects of ZC 50 NCs on the L929 fibroblast cell line, as evaluated by the MTT assay.

## Antimicrobial studies

*In vitro* antimicrobial activity of ZC 10, ZC 20, ZC 30, and ZC 50 NCs was performed against Gram-negative (*E. coli* NCIM 2832, *P. aeruginosa*, NCIM 5032) and Gram-positive (*B. cereus* 2703, *S. aureus* NCIM 2654) bacterial strains and *C. albicans* fungal strains by modified agar well diffusion method.[48,49] The suspension of respective test pathogens was prepared in sterile saline and used for further study. For the antimicrobial activity test, pathogens were inoculated on the surface of sterile Mueller and Hinton agar and spread on plates using a sterile spreader. After that agar well was prepared aseptically with the help of a sterilized cork borer having a 0.7 cm diameter. Then 100 μL volumes of the test sample [concentration 100 μg mL$^{-1}$ of respective test compound] were added to the different wells of the respective test pathogens. Then plates were placed at 4 °C for 20 min for sample diffusion in a culture medium and transferred to an incubator at 37 °C for 24 h.

The antibacterial activity of ZC NCs is driven by a synergistic mechanism involving both physical disruption and biochemical interactions. Upon exposure to light or aqueous environments, ZnO NRs and CuO NFs generate ROS such as hydroxyl radicals, superoxide anions, and hydrogen peroxide, which induce oxidative stress, lipid peroxidation, protein damage, and DNA fragmentation in bacterial cells.[43] Additionally, the sharp morphology of the NCs physically disrupts bacterial membranes, increasing permeability and causing cytoplasmic leakage.[1] The release of $Zn^{2+}$ and $Cu^{2+}$ ions further interferes with enzymatic functions, binds to essential biomolecules, and disrupts metabolic and replication processes. Collectively, these mechanisms lead to effective bacterial inactivation, making ZC NCs potent antimicrobial agents against both Gram-positive and Gram-negative bacteria.[50]

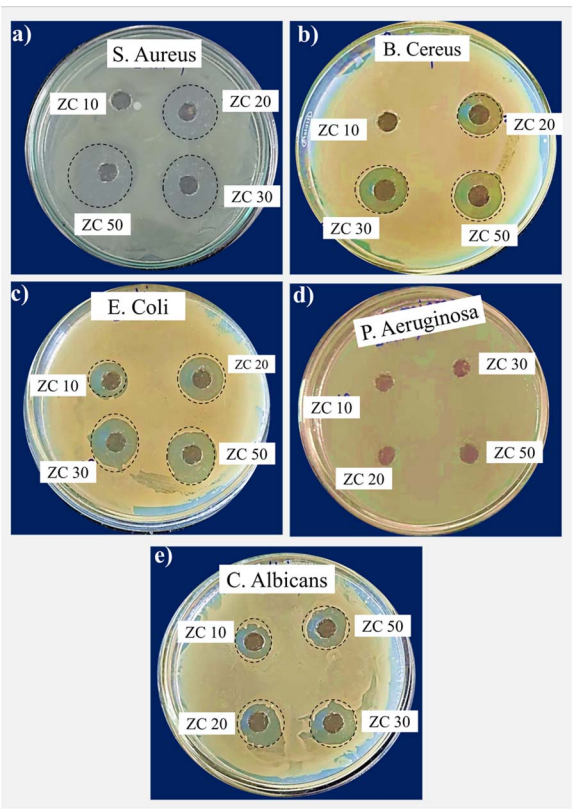


Fig. 7 Zone of inhibition of ZC 10, ZC 20, ZC 30, and ZC 50 NCs against (a) *S. aureus*, (b) *B. cereus*, (c) *E. coli*, (d) *P. aeruginosa*, and (e) *C. albicans*.

Furthermore, the obtained results were compared with the well containing streptomycin (1000 μg $mL^{-1}$) as a positive control, and sterile distilled water was kept as a negative control. The diameter of the inhibition zone was measured in mm, and the results were recorded as follows. ZC 50 NCs shows good antibacterial and antifungal activity against test pathogens except *P. aeruginosa*.

For the antifungal activity evaluation, a comparable procedure was adopted. MGYP (Malt Extract, Glucose, Yeast Extract, and Peptone) agar plates were prepared and inoculated using the submerged inoculation technique with the specified fungal strains. The inoculated plates were incubated at 27 °C for 48 to 72 h. After incubation, the plates were examined for clear zones around the wells, indicating antifungal activity. The results were compared against the standard antifungal drug ketoconazole (100 μg $mL^{-1}$) as a positive control, while sterile distilled water was used as a negative control. The inhibition zone diameters were measured in millimeters, as presented in Fig. 7a–e and summarized in Table 4. Additionally, the zone of inhibition for ZnO NRs and CuO NFs against *S. aureus* and *C. albicans* is shown in Fig. S6 (SI) and detailed in Table S4.

Among the tested samples, ZC 50 NCs exhibited notable antibacterial activity against *Bacillus cereus* and antifungal activity against *Candida albicans*, whereas ZC 10 NCs displayed limited effectiveness. *P. aeruginosa* showed no zone of inhibition, likely due to the inadequate diffusion of antimicrobial agents in the agar medium and the presence of multidrug efflux pumps (such as MexAB–OprM), which actively expel antibacterial agents.[51] The inhibition zone diameters for streptomycin and ketoconazole against the respective test pathogens are summarized in Table 5.

A comparison of the antibacterial activity of our synthesized ZC 50 NCs with previously reported metal oxide nanoparticles and their NCs would provide a clearer context and highlight the significance of our results (Table 6). The enhanced antibacterial activity of ZC 50 NCs arises from their synergistic properties. Both ZnO and CuO generate ROS and release antimicrobial $Zn^{2+}$ and $Cu^{2+}$ ions. Their combination improves electron hole separation, boosting ROS production ($^{\bullet}OH$, $O_2^{\bullet-}$, $H_2O_2$), which damages bacterial membranes, proteins, and DNA. The NRs and NFs morphologies provide a high surface area and active sites for better microbial interaction. The ZC heterojunction and surface defects further enhance charge separation and ROS activity. Compared to Ag–$TiO_2$, CuO–$TiO_2$, or ZnO–NiO, ZC 50 NCs shows superior antimicrobial efficacy due to this multi-mechanistic action.

Table 4 Zone of inhibition of NCs against various concentrations of respective test pathogens

| | Nanocomposites zone of inhibition in mm | | | |
|---|---|---|---|---|
| | Concentration (100 μg $mL^{-1}$) | | | |
| Test pathogens | ZC 10 | ZC 20 | ZC 30 | ZC 50 |
| *B. cereus* | 00 | 19 | 22 | 25 |
| *S. aureus* | 00 | 18 | 21 | 24 |
| *E. coli* | 15 | 19 | 20 | 23 |
| *P. aeruginosa* | 00 | 00 | 00 | 00 |
| *C. albicans* | 12 | 18 | 21 | 22 |

Table 5 Zone of inhibition of streptomycin and ketoconazole against respective test pathogens

| | Zone of inhibition (mm) | | |
|---|---|---|---|
| Test pathogens | Streptomycin | Ketoconazole | DMSO |
| *B. cereus* | 00 | 19 | 22 |
| *S. aureus* | 00 | 18 | 21 |
| *E. coli* | 15 | 19 | 20 |
| *P. aeruginosa* | 00 | 00 | 00 |
| *C. albicans* | 12 | 18 | 21 |

## Protein leakage assay

The protein leakage from the entire cell of the pathogenic bacterium *B. cereus* (NCIM 2703) was analyzed using the Bradford assay.[60] A suspension of 18 h old bacterial cells with a cell density of $1 \times 10^5$ was prepared in 3 mL of sterile nutrient broth. The suspension was then treated with 100 μL of ZC 50 NCs at a concentration of 100 μg $mL^{-1}$ for 12 h, and the mixture was incubated at 37 °C. After incubation, the tubes were centrifuged at 7000 rpm for 20 minutes, and the cell-free broth was collected for protein estimation. A similar procedure was conducted for the control, where no ZC 50 NCs were added. For protein estimation, 0.5 mL of the cell-free broth was taken and

Table 6 Comparative analysis of zone of inhibition for synthesized ZC NCs from previous studies

| Sr. no. | Samples | Synthesis methods | Zone of inhibition (mm) | Ref. |
|---|---|---|---|---|
| 1 | ZnO | Probe sonication | 14.5 | 52 |
| 2 | CuO | Green synthesis | 18 | 53 |
| 3 | Ag–$TiO_2$ | Ultrasonication | 11 | 54 |
| 4 | Ag–ZnO | Green synthesis | 19 | 55 |
| 5 | ZnO–NiO | PLAL | 20 | 56 |
| 6 | ZnO–$TiO_2$ | Sol–gel | 19.7 | 57 |
| 7 | $Bi_2O_3$–CuO–GO | Co-precipitation | 18 | 58 |
| 8 | ZnO–CuO | Co-precipitation | 15 | 59 |
| 9 | $TiO_2$–CuO/GO | Hydrothermal | 22 | 13 |
| 10 | ZnO–CuO | Sol–gel | 25 | Present study |

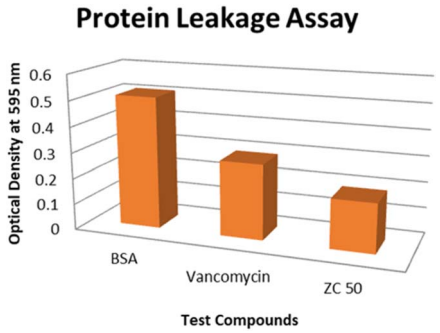


Fig. 8 Protein leakage assay in the presence of ZC 50 NCs.

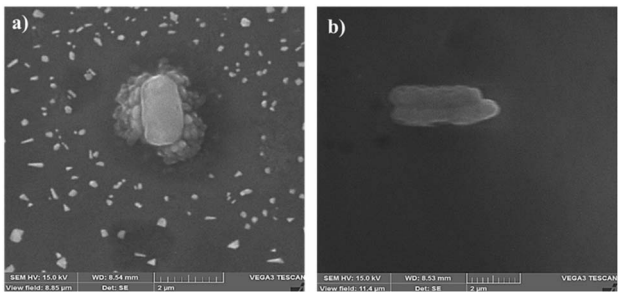


Fig. 9 SEM images of *B. cereus* cells treated with ZC 50 NCs showing (a) control sample: after scanning it shows the outer membrane intact, (b) test image: after scanning it shows rupture in outer membrane *i.e.* cell wall.

treated with Bradford reagent, then incubated in the dark for 10 minutes. The optical density of the sample was measured at 595 nm. Bovine serum albumin (BSA) at a concentration of 250 μg $mL^{-1}$ was used as the standard protein.

The protein leakage assay (Fig. 8) revealed that ZC 50 NCs exhibit significant antimicrobial activity against *B. cereus* (NCIM 2703), comparable to the standard antibiotic vancomycin. These findings provide further insight into the mode of action of ZC 50 NCs on bacterial cells, as supported by SEM studies provide valuable insights into the mechanism of action of ZC 50 NCs on bacterial cells.

### Mode of action study

The mechanism of antibacterial activity was investigated to understand the interactions of the NCs with microbial cells. It is hypothesized that ZC NCs generate ROS upon interaction with bacterial membranes, leading to oxidative stress, lipid peroxidation, and disruption of the cell membrane integrity.[61] Additionally, the NCs can interfere with cellular processes by binding to proteins and nucleic acids, further inhibiting bacterial or fungal growth. The dual-action mechanism of physical damage to the membrane and biochemical disruption likely contributes to the potent antibacterial as well as antifungal effects observed.[62] To study the mode of action of ZC 50 NCs, *B. cereus* was used as an indicator microorganism. Bacteria in the mid-exponential growth phase were diluted with sterile nutrient agar medium to the desired cell density and then treated with the test NCs at a concentration that produced a high zone of inhibition (ZC 50; see Table 3) for 4 h at 37 °C. An untreated control was prepared using both standard and sterile nutrient broth and incubated under the same conditions. After incubation, both test and control samples were centrifuged at 8000 rpm for 10 minutes. The supernatant was discarded, and the resulting pellet was resuspended in sterile Milli-Q water for SEM sample preparation on grease-free slides.

SEM samples were prepared on 1 cm × 1 cm grease-free slides, with bacteria fixed using 2% glutaraldehyde. A drop of glutaraldehyde was placed on each slide square, followed by 10 μL of control and test samples applied to the drop using a micropipette [Hi-Media]. The slides were shade-dried in a closed container and then stored at 4 °C overnight. The samples were subsequently dehydrated through a graded ethanol series (10–100%) and air-dried. Microscopy was then performed, and images were captured. Fig. 9a and b shows SEM images of *B. cereus* cells treated with ZC 50 NCs. The scanning of the control sample showed intact *B. cereus* cells, while the test sample (ZC 50 NCs) displayed ruptured cells, indicating cell wall disruption. This suggests that the synthesized ZC 50 NCs compromise cell wall integrity, leading to cell wall destabilization, leakage of cell contents, and eventual death of the test pathogen.[63]

## Experimental section

### Materials

All chemicals used were of analytical grade and were utilized as received without further purification. All media components and chemicals required for antimicrobial and mode of action studies were purchased from Hi-Media India and Sigma Aldrich.

The synthetic protocols for the synthesis of bare ZnO NRs[64] and CuO NFs[65] are described in SI.

### Synthesis of ZnO–CuO NCs

ZC NCs were prepared using an *in situ* sol–gel route with a variable content of CuO NFs (10, 20, 30, and 50 wt%). Synthesized CuO NFs were added immediately after the complete precipitation of zinc hydroxide [$Zn(OH)_2$] within the running route of ZnO NRs synthesis, as shown in Scheme 1. The final black-colored precipitates were washed three times with double-distilled water (DDW) and twice with ethanol to remove impurities and by-products formed during the reaction. The washed product was then dried in a hot air oven at 80 °C until completely dry, followed by calcination at 400 °C for 4 h. The synthesized samples were assigned as ZC 10, ZC 20, ZC 30, and ZC 50 NCs, having CuO NFs content of 10, 20, 30, and 50 wt%, respectively.

### Characterization tools

The powder XRD patterns of the samples were obtained using a Bruker AXS D8 Advance diffractometer. FT-IR spectra were recorded on a Bruker ALPHA FT-IR spectrometer. The optical properties were examined using UV-visible DRS, measured with a LABINDIA UV 3092 spectrophotometer. Raman spectra were obtained with a Bruker MultiRAM Raman spectrometer. FESEM

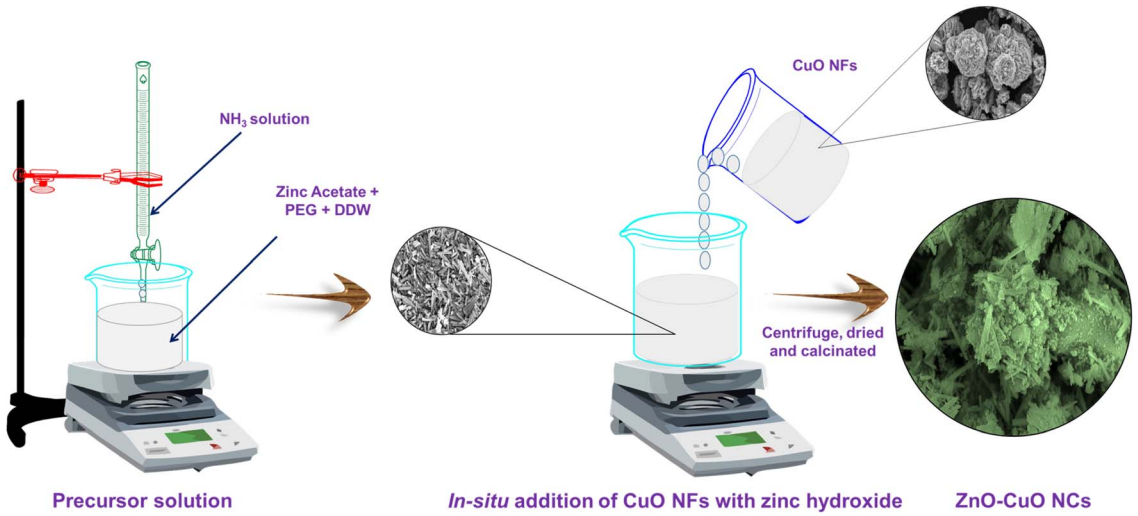


Scheme 1 Schematic representation of the synthetic protocol for ZC NCs.

images were captured using a JEOL JSM-6360 FESEM along with EDS for morphological and elemental composition analysis. Surface area and pore size measurements were conducted using a BET surface analyzer (Quantachrome NOVA1000e, USA).

## Conclusions

This study efficaciously synthesized various ZC NCs in varying compositions by functionalizing ZnO NRs with CuO NFs. Among these, ZC 50 NCs exhibited the highest antimicrobial performance, providing valuable insights into their mode of action. Controlled synthesis and detailed physicochemical characterization confirmed the structural integrity and enhanced surface properties of the NCs, with ZC 50 NCs (containing 50 wt% CuO) demonstrating the highest surface area (187.622 $m^2 g^{-1}$). EDS analysis verified elemental composition, while FESEM imaging revealed the distinct morphologies of ZnO (nanorods) and CuO (nanoflowers). These structural attributes contributed to the NCs' potent antimicrobial activity, primarily driven by bacterial membrane disruption and oxidative stress mechanisms. The ZC NCs exhibited broad-spectrum efficacy against clinically relevant pathogens, including *S. aureus*, *B. cereus*, *E. coli*, and *P. aeruginosa*, along with the fungal strain *C. albicans*. Mechanistic investigations using SEM imaging confirmed microbial cell wall damage, while cytotoxicity assessments indicated minimal adverse effects, reinforcing their suitability for biomedical applications. The findings highlight ZC NCs as scalable and cost-effective materials with significant potential for diverse applications, including coatings for medical devices and implants, wound dressings, surface disinfection, and water purification. Future research should focus on evaluating their long-term stability and real-world performance to further expand their applicability in healthcare. This study underscores the potential of ZC NCs as promising solutions for addressing current challenges in antimicrobial resistance and infection control.

## Author contributions

Authors V. S. G. and P. A. K. contributed equally to this work. V. S. G. designed the experimental work and performed the antibacterial study, which S. D. D. reviewed. S. S. P. and P. S. P. contributed to the Rietveld analysis. Thereafter, V. S. G. and P. A. K. analyzed the data and interpreted the results. In addition, V. S. G. and P. A. K. wrote the whole manuscript and further reviewed it by S. D. D.

## Conflicts of interest

There are no conflicts to declare.

## Data availability

The data supporting this article have been included as part of the SI. Supplementary information: synthesis of ZnO NRs and CuO NFs, XRD patterns of ZnO, CuO, and ZC NCs, FT-IR, UV-visible DRS, and Tauc plot of ZC NCs, BJH analysis for ZnO NRs and ZC 50 NCs, zone of inhibition of ZnO NRs and CuO NFs, *etc.* See DOI: **https://doi.org/10.1039/d5ra04095g**.

## References

1 R. Dadi, R. Azouani, M. Traore, C. Mielcarek and A. Kanaev, *Mater. Sci. Eng., C*, 2019, **104**, 109968.
2 G. Micheli, F. Sangiorgi, F. Catania, M. Chiuchiarelli, F. Frondizi, E. Taddei and R. Murri, *Microorganisms*, 2023, **11**, 1–19.
3 S. K. Mondal, S. Chakraborty, S. Manna and S. M. Mandal, *RSC Pharm.*, 2024, **1**, 388–402.
4 M. S. Butler, W. Vollmer, E. C. A. Goodall, R. J. Capon, I. R. Henderson and M. A. T. Blaskovich, *ACS Infect. Dis.*, 2024, **10**, 3440–3474.
5 T. Vitasovic, G. Caniglia, N. Eghtesadi, M. Ceccato, E. D. Bøjesen, U. Gosewinkel, G. Neusser, U. Rupp,

P. Walther, C. Kranz and E. E. Ferapontova, *ACS Appl. Mater. Interfaces*, 2024, **16**, 30847–30859.
6 S. Fu, Y. Zhang, G. Qin and E. Zhang, *Mater. Sci. Eng., C*, 2021, **128**, 112266.
7 F. A. Bezza, S. M. Tichapondwa and E. M. N. Chirwa, *Sci. Rep.*, 2020, **10**, 1–18.
8 A. Frei, A. D. Verderosa, A. G. Elliott, J. Zuegg and M. A. T. Blaskovich, *Nat. Rev. Chem.*, 2023, **7**, 202–224.
9 S. Prabhu, T. Daniel Thangadurai, P. Vijai Bharathy and P. Kalugasalam, *Results Chem.*, 2022, **4**, 100285.
10 H. F. Etefa, D. J. Nemera and F. B. Dejene, *ACS Omega*, 2023, **8**, 38418–38425.
11 F. Hajareh Haghighi, M. Mercurio, S. Cerra, T. A. Salamone, R. Bianymotlagh, C. Palocci, V. Romano Spica and I. Fratoddi, *J. Mater. Chem. B*, 2023, **11**, 2334–2366.
12 V. Kumaravel, K. M. Nair, S. Mathew, J. Bartlett, J. E. Kennedy, H. G. Manning, B. J. Whelan, N. S. Leyland and S. C. Pillai, *Chem. Eng. J.*, 2021, **416**, 129071.
13 C. Thambiliyagodage, H. Liyanaarachchi, M. Jayanetti, G. Ekanayake, A. Mendis, U. Samarakoon and S. Vigneswaran, *Sci. Rep.*, 2024, **14**, 1–23.
14 M. S. Hassan, T. Amna, H. Y. Kim and M. S. Khil, *Composites, Part B*, 2013, **45**, 904–910.
15 S. B. Dhage, P. M. Sah, J. Lakkakula, R. W. Raut, Y. S. Malghe, A. Roy, D. Verma and K. Kaur, *Biointerface Res. Appl. Chem.*, 2024, **14**, 3.
16 T. Jan, S. Azmat, Q. Mansoor, H. M. Waqas, M. Adil, S. Z. Ilyas, I. Ahmad and M. Ismail, *Microb. Pathog.*, 2019, **134**, 103579.
17 M. Azizi-Lalabadi, A. Ehsani, B. Divband and M. Alizadeh-Sani, *Sci. Rep.*, 2019, **9**, 1–10.
18 A. Negi, S. Ringwal, M. Pandey and M. Taha Yassin, *Sci. Rep.*, 2024, **14**, 1–14.
19 L. Ye, X. He, E. Obeng, D. Wang, D. Zheng, T. Shen, J. Shen, R. Hu and H. Deng, *Mater. Today Bio*, 2023, **18**, 100552.
20 I. A. Hassan, S. Sathasivam, S. P. Nair and C. J. Carmalt, *ACS Omega*, 2017, **2**, 4556–4562.
21 N. Babayevska, Ł. Przysiecka, I. Iatsunskyi, G. Nowaczyk, M. Jarek, E. Janiszewska and S. Jurga, *Sci. Rep.*, 2022, **12**, 1–13.
22 Y. Matsuda, K. Okuyama, H. Yamamoto, M. Fujita, S. Abe, T. Sato, N. Yamada, M. Koka, H. Sano, M. Hayashi, S. K. Sidhu and T. Saito, *Nucl. Instrum. Methods Phys. Res., Sect. B*, 2019, **458**, 184–188.
23 E. Takele, R. Feyisa Bogale, G. Shumi and G. Kenasa, *J. Chem.*, 2023, **1**, 3481389.
24 C. Prakash, R. Chaurasiya, A. J. Kale and A. Dixit, *ACS Omega*, 2022, **7**, 28206–28216.
25 R. Pachaiappan, S. Rajendran, P. L. Show, K. Manavalan and M. Naushad, *Chemosphere*, 2020, 128607.
26 M. Jayanetti, C. Thambiliyagodage, H. Liyanaarachchi, G. Ekanayake, A. Mendis and L. Usgodaarachchi, *Sci. Rep.*, 2024, **14**, 1–21.
27 M. Pandey, M. Singh, K. Wasnik, S. Gupta, S. Patra, P. S. Gupta, D. Pareek, N. S. N. Chaitanya, S. Maity, A. B. M. Reddy, R. Tilak and P. Paik, *ACS Omega*, 2021, **6**, 31615–31631.
28 C. M. Magdalane, K. Kaviyarasu, J. J. Vijaya, B. Siddhardha and B. Jeyaraj, *J. Photochem. Photobiol., B*, 2016, **163**, 77–86.
29 G. A. Govindasamy, R. B. S. M. N. Mydin, S. Sreekantan and N. H. Harun, *Sci. Rep.*, 2021, **11**, 1–14.
30 S. B. Dhage, P. M. Sah, J. Lakkakula, R. W. Raut, Y. S. Malghe, A. Roy, D. Verma and K. Kaur, *Biointerface Res. Appl. Chem.*, 2024, **14**, 1–10.
31 A. Al Baroot, M. Alheshibri, Q. A. Drmosh, S. Akhtar, E. Kotb and K. A. Elsayed, *Arabian J. Chem.*, 2022, **15**, 103606.
32 A. Yousefinia, M. Khodadadi and S. Mortazavi-Derazkola, *Environ. Technol. Innovation*, 2023, **32**, 103340.
33 K. S. Mamatha, H. M. Suresh Kumar, T. D. Puttaraju, T. L. Soundarya and G. Nagaraju, *Ionics*, 2024, **30**, 7665–7684.
34 A. Mengistu, M. Naimuddin and B. Abebe, *RSC Adv.*, 2023, **13**, 24835–24845.
35 F. A. Alharthi, A. A. Alghamdi, N. Al-Zaqri, H. S. Alanazi, A. A. Alsyahi, A. El Marghany and N. Ahmad, *Sci. Rep.*, 2020, **10**, 1–14.
36 S. M. Pawar, S. S. Patil, K. D. Sonawane, V. B. More and P. S. Patil, *Surf. Interfaces*, 2024, **51**, 104598.
37 A. Sirelkhatim, S. Mahmud, A. Seeni, N. H. M. Kaus, L. C. Ann, S. K. M. Bakhori, H. Hasan and D. Mohamad, *Nano-Micro Lett.*, 2015, **7**, 219–242.
38 N. Padmavathy and R. Vijayaraghavan, *Sci. Technol. Adv. Mater.*, 2008, **9**, 035004.
39 K. Fatima, M. Asif, U. Farooq, S. J. Gilani, M. N. Bin Jumah and M. M. Ahmed, *ACS Omega*, 2024, **9**, 15882–15892.
40 D. M. Nzilu, E. S. Madivoli, D. S. Makhanu, S. I. Wanakai, G. K. Kiprono and P. G. Kareru, *Sci. Rep.*, 2023, **13**, 1–18.
41 A. Ali, S. R. Ali, R. Hussain, R. Anjum, Q. Liu, M. S. Elshikh, N. Alkubaisi, R. Iqbal, S. Tabor and M. Gancarz, *Sci. Rep.*, 2025, **15**, 1–16.
42 P. A. Koyale, S. P. Kulkarni, J. L. Gunjakar, T. D. Dongale, S. S. Sutar, S. S. Soni, Y. G. Kapdi, S. V Mulik and S. D. Delekar, *ACS Appl. Nano Mater.*, 2024, **7**, 2662–2676.
43 S. Qiu, H. Zhou, Z. Shen, L. Hao, H. Chen and X. Zhou, *RSC Adv.*, 2020, **10**, 2767–2785.
44 R. B. Asamoah, E. Annan, B. Mensah, P. Nbelayim, V. Apalangya, B. Onwona-Agyeman and A. Yaya, *Adv. Mater. Sci. Eng.*, 2020, **1**, 7814324.
45 S. N. Kane, A. Mishra and A. K. Dutta, *J. Phys.: Conf. Ser.*, 2016, **755**(1), 011001.
46 I. Georgakopoulos-Soares, E. L. Papazoglou, P. Karmiris-Obratański, N. E. Karkalos and A. P. Markopoulos, *Colloids Surf., B*, 2023, **231**, 113584.
47 R. P. Pal Singh, I. S. Hudiara and S. B. Rana, *Mater. Sci.-Pol.*, 2016, **34**, 451–459.
48 M. Hartmann, M. Berditsch, J. Hawecker, M. F. Ardakani, D. Gerthsen and A. S. Ulrich, *Antimicrob. Agents Chemother.*, 2010, **54**, 3132–3142.
49 L. Scorzoni, F. Sangalli-Leite, J. de Lacorte Singulani, A. C. A. de Paula e Silva, C. B. Costa-Orlandi, A. M. Fusco-Almeida and M. J. S. Mendes-Giannini, *J. Microbiol. Methods*, 2016, **123**, 68–78.
50 U. S. Ezealigo, B. N. Ezealigo, S. O. Aisida and F. I. Ezema, *JCIS Open*, 2021, **4**, 100027.

51 Z. Pang, R. Raudonis, B. R. Glick, T. J. Lin and Z. Cheng, *Biotechnol. Adv.*, 2019, **37**, 177–192.
52 N. B. Raj, N. T. PavithraGowda, O. S. Pooja, B. Purushotham, M. R. A. Kumar, S. K. Sukrutha, C. R. Ravikumar, H. P. Nagaswarupa, H. C. A. Murthy and S. B. Boppana, *J. Photochem. Photobiol.*, 2021, **6**, 100021.
53 M. Palani, S. Kalaiselvan, J. A. Martin Mark, K. Chandran and V. Ekhambaram, *Asp. Mol. Med.*, 2024, **4**, 100049.
54 S. P. Deshmukh, V. B. Koli, A. G. Dhodamani, S. M. Patil, V. S. Ghodake and S. D. Delekar, *ChemistrySelect*, 2021, **6**, 113–122.
55 S. G. Mtavangu, R. L. Machunda, B. van der Bruggen and K. N. Njau, *Sci. Rep.*, 2022, **12**, 1–14.
56 H. J. Imran, K. A. Hubeatir and K. A. Aadim, *Sci. Rep.*, 2023, **13**, 1–13.
57 M. M. Ali, M. J. Haque, M. H. Kabir, M. A. Kaiyum and M. S. Rahman, *Results Mater.*, 2021, **11**, 100199.
58 A. Qayyum, Z. Batool, M. Fatima, S. A. Buzdar, H. Ullah, A. Nazir, Q. Jabeen, S. Siddique and R. Imran, *Sci. Rep.*, 2022, **12**, 1–19.
59 S. B. Dhage, P. M. Sah, J. Lakkakula, R. W. Raut, Y. S. Malghe, A. Roy, D. Verma and K. Kaur, *Biointerface Res. Appl. Chem.*, 2024, **14**, 1–10.
60 S. Shankar and R. S. Laxman, *Appl. Biochem. Biotechnol.*, 2015, **175**, 589–602.
61 K. Karthik, S. Dhanuskodi, C. Gobinath, S. Prabukumar and S. Sivaramakrishnan, *J. Mater. Sci.: Mater. Electron.*, 2018, **29**, 5459–5471.
62 N. T. Tasnim, N. Ferdous, M. M. H. Rumon and M. S. Shakil, *ACS Omega*, 2024, **9**, 16–32.
63 M. Khan, M. N. Tahir, S. F. Adil, H. U. Khan, M. R. H. Siddiqui, A. A. Al-Warthan and W. Tremel, *J. Mater. Chem. A*, 2015, **3**, 18753–18808.
64 V. S. Ghodake, P. A. Koyale and S. D. Delekar, *ChemistrySelect*, 2025, **10**, 1–12.
65 V. S. Ghodake, P. A. Koyale, V. B. More, K. D. Sonawane and S. D. Delekar, *RSC Adv.*, 2025, **15**, 2591–2601.